atmosphere

MDPI

Article

Precipitation Microphysical Characteristics of Typhoon Mangkhut in Southern China Using 2D Video Disdrometers

Lu Feng [1], Sheng Hu [1], Xiantong Liu [1,*], Hui Xiao [1], Xiao Pan [2], Feng Xia [1], Guanhua Ou [3] and Chu Zhang [4]

1 Guangzhou Institute of Tropical and Marine Meteorology, China Meteorological Administration, Guangzhou 510641, China; fengl@gd121.cn (L.F.); sheng_hu@gd121.cn (S.H.); xiaoh@gd121.cn (H.X.); xiaf@gd121.cn (F.X.)
2 Institute of Atmospheric Environment, China Meteorological Administration, Shenyang 110166, China; panxiao1@mail.ustc.edu.cn
3 Xinfeng Meteorological Bureau, China Meteorological Administration, Xinfeng, Guangdong 512028, China; 13927876880@139.com
4 Jiangmen Meteorological Bureau, China Meteorological Administration, Jiangmen, Guangdong 529000, China; qxt121@126.com
* Correspondence: xtliu@gd121.cn

Received: 3 August 2020; Accepted: 8 September 2020; Published: 11 September 2020

Abstract: The microphysical characteristics of tropical cyclones vary in different rain regions, which affects not only the dynamic and thermodynamic mechanisms of the typhoon system but also the development of tropical cyclones. This study analyzed the raindrop size distribution (DSD) and the gamma DSD parameters associated with Typhoon Mangkhut using three two-dimensional (2D) video disdrometers from the Longmen Field Experiment Base for Cloud Physics, China Meteorological Administration in Guangdong, China during 16–17 September 2018. According to the observed track and radar reflectivity, this process can be divided into three distinct segments: the outer rainband before landfall (S1), the inner core (S2), and the outer rainband after landfall (S3). The outer rainband mainly produces stratiform rains, while the inner core mainly produces convective rains. The temporal and spatial variations in the rain rate, radar reflectivity, and DSD parameters of the different segments were analyzed and compared at three sites. Although the DSD characteristics are distinctly different in the three segments, the DSD characteristics of the same segment were similar at different sites. In the inner core (S2), the precipitation contains smaller drops (around 0.5 mm) and the concentrations are higher within each size bin compared with those of the other segments, resulting in the maximum rain rate (11.66 mm h^{-1}), radar reflectivity (34.53 dBZ), liquid water content (0.65 g m^{-3}), and number concentration (4.12 mm^{-1} m^{-3} on a logarithmic scale) occurring in this segment. The N_w–D_m scatter pairs have maritime-like convection, which increases outward from the inner core (S2). The relationship between the shape (μ) and slope (Λ) was also investigated. The microphysical characteristics determined in this study provide useful information for understanding microphysical precipitation processes and for improving the precision of numerical weather prediction models.

Keywords: Typhoon Mangkhut; 2D video disdrometer; raindrop size distribution; microphysics; precipitation

1. Introduction

The raindrop size distribution (DSD) is a key parameter for cloud and precipitation microphysical process analysis, which is essential for creating numerical weather prediction models [1,2].

The variations in the DSD are also important to quantitative precipitation estimation (QPE) and forecasting (QPF) based on polarimetric radar [3,4].

In the past, conventional measurement techniques, including the momentum method, the flour method, filter paper, raindrop camera, and the immersion method, have been used to collect and determine the DSD parameters artificially. However, these methods have many disadvantages, such as measurement error, a heavy workload, and low efficiency [5]. To develop a faster technique, the Joss–Waldvogel (JW) disdrometer, the optical disdrometer, and the acoustic disdrometer were invented [6–10]. Use of the optical disdrometer is widespread now, including the one-dimensional disdrometer (such as the Parsivel) and the two-dimensional (2D) disdrometer (such as the 2D Video Disdrometer, 2DVD). Moreover, Raupach et al. [11] presented a method that improved the accuracy of the DSD measurements recorded using the Parsivel by using a 2DVD as a reference instrument. Compared with the Parsivel, the 2DVD can effectively avoid the particle superposition errors because it performs high-speed scanning in two mutually perpendicular directions and obtains accurate, high-resolution DSD parameters (particle shape, diameter, axial ratio, and size distribution) vertically and horizontally [12,13]. However, the 2DVD is rarely used to obtain the microphysical characteristics of precipitation particles in China because it is quite expensive [14]. Several 2DVDs have been built in the Longmen Field Experiment Base for Cloud Physics, China Meteorological Administration, in recent years, for the in-depth investigation of microphysical precipitation processes.

Based on the JW disdrometer, the DSDs of seven tropical cyclones in the United States were found to exhibit high concentrations of both small and midsize drops [15]. Chen et al. [16] focused on the DSD of a typhoon in Fujian Province, China, using a Parsivel. They found that the stratiform rain consisted of rimed ice particles and the melting of graupel in the outer rainband and eye region. Based on the 2DVD and C-band polarimetric radar, Chang et al. [17] investigated the DSDs and drop shape relations (DSR) of typhoon systems during landfall in the western Pacific. They determined that the DSDs collected by the 2DVD were located between the maritime and continental clusters, which were defined by Bringi et al. [18], while exhibiting a maritime convective type over the ocean based on the C-band polarimetric radar. During the passage of Typhoon Matmo over Eastern China, Wang et al. [19] investigated the DSDs of the different stages of the typhoon using an S-band polarimetric radar and a 2DVD. Furthermore, the convective rain was compared by Bringi et al. [18]. Based on the 2DVD and C-band polarimetric radar data, Wen et al. [20] attempted to investigate the DSD and DSR of seven typhoons in China. They found that although the DSDs of the seven typhoons differed, the microphysical characteristics of two of the typhoons were similar. Bao et al. [21] studied the DSDs of the different rainbands of Typhoon Fitow during landfall in Eastern China using a Parsivel. Moreover, they demonstrated that the evolutions of the DSDs with increasing rain rate in the different convective rainbands were completely different.

Previous studies have investigated the DSD characteristics of different rain types of different precipitation systems in different rain regions [20–24]. Several scholars have focused on the DSD characteristics of tropical cyclone precipitation systems before and after landfall [25,26]. Heavy rainfall events are common in Southern China, and they frequently cause financial loss and endanger people's lives and societal security. Although various scholars have investigated the DSDs of typhoon systems, they are still poorly studied in Southern China, and few studies have focused on the different horizontal and spatial distributions of typhoons. In this study, we focus on the DSD characteristics of Typhoon Mangkhut as it made landfall over Southern China using a 2DVD, revealing that it had unique dynamic and microphysical characteristics. Moreover, the different rain regions in numerical weather prediction models may require different microphysical parameterization schemes.

2. Data and Methods

2.1. Instruments and Dataset

In this study, the datasets were collected using the 2DVD from the Longmen Field Experiment Base for Cloud Physics, China Meteorological Administration. The three 2DVDs at the Enping (EP), Fogang (FG), and Xinfeng (XF) sites were used during Typhoon Mangkhut's passage over Guangdong on 16–17 September 2018 (Figure 1). The 2DVDs performed high-speed scanning with light line arrays in two mutually perpendicular directions (55 kHz). The rectangular sample area was about 10×10 cm^2, and the sampling interval of the particle sizes was 0.2 mm (from 0.1 to 8.1 mm) in diameter. The details of the 2DVD instrument can be found at www.distrometer.at.

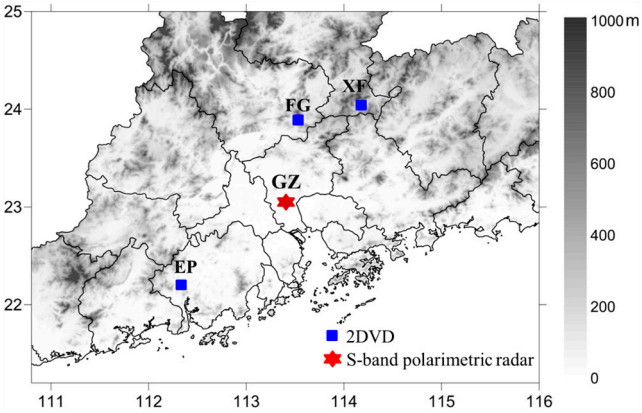

Figure 1. The geographic locations of the instruments in Guangdong used in this study. The three 2D Video Disdrometer (2DVDs) were located at the Enping (EP), Fogang (FG), and Xinfeng (XF) sites. The S-band polarimetric radar was located at the Guangzhou (GZ) site.

First, the 2DVD data were processed into a one-minute resolution dataset, and then, its quality was controlled using Tokay's method [27]. For every 1 minute, if the rain rate was less than 0.1 mm h^{-1} or the total number of raindrops was less than 10, the data point was removed to ensure data quality. The processed 2DVD observation data are consistent with that of a rain gauge, which has been assessed by Feng et al. [28]. Moreover, the number concentration of raindrops with diameters in the range of a unit size interval $N(D_i)$ is calculated as follows:

$$N(D_i) = \sum_{i=1}^{41} \sum_{j=1}^{n(i)} \frac{1}{A \cdot \Delta t \cdot V_{i,j} \cdot \Delta D_i} \tag{1}$$

where A is the effective sampling area (about 10×10 cm^2); Δt is the sampling time (1 min); $V_{i,j}$ (m s^{-1}) is the fall speed in the ith size bin and in the number of raindrops bin j; $n(i)$ is the number of raindrops in each bin; and ΔD_i is the sampling interval of the particle sizes (0.2 mm).

In addition, an S-band polarimetric radar was used to collect the radar reflectivity at the Guangzhou site (GZ). The S-band polarimetric radar simultaneously transmits and receives horizontally and vertically polarized scattered signals with the resolution range increasing from 1000 to 250 m. The S-band polarimetric radar was processed into a six-minute resolution dataset, and its quality was controlled using the method of Liu [13].

2.2. 2DVD Data Processing

The gamma distribution of the DSDs is expressed as

$$N(D) = N_0 D^{\mu} \exp(-\Lambda D) \tag{2}$$

where N_0 (mm^{-1} m^{-3}) is the intercept; μ is the shape; and Λ (mm^{-1}) is the slope. The curve decreases when $\mu > 0$, and it increases when $\mu < 0$. When $\mu = 0$, it degenerates into an exponential distribution. The exponential distribution with $N_0 = 8000$ mm^{-1} m^{-3} is known as the Marshall–Palmer DSD [29].

When $N(D_i)$ is calculated using Equation (1), the radar reflectivity factor Z (mm^6 m^{-3}), the rain rate R (mm h^{-1}), the liquid water content LWC (g m^{-3}), and the total raindrop number concentration N_t (m^{-3}) can be calculated using the following equations:

$$Z = \sum_{i=1}^{L} D_i^6 N(D_i) \Delta D_i \tag{3}$$

$$R = \frac{6\pi}{10^4} \sum_{i=1}^{L} D_i^3 V_i N(D_i) \Delta D_i \tag{4}$$

$$LWC = \frac{\pi}{6000} \sum_{i=1}^{L} D_i^3 N(D_i) \Delta D_i \tag{5}$$

$$N_t = \sum_{i=1}^{L} N(D_i) \Delta D_i \tag{6}$$

where L is the total number of bins ($L = 41$); D_i (mm) is the equivalent spherical raindrop diameter in the ith size bin; ΔD_i (mm) is the corresponding diameter interval; and V_i (m s^{-1}) is the fall speed in velocity bin i. $N(D_i)$ (mm^{-1} m^{-3}) is the number concentration of raindrops with diameters in the range of $D_i - 0.5\Delta D_i$ to $D_i + 0.5\Delta D_i$ (per unit size interval).

The nth-order moment of the DSD is defined as

$$M_n = \int_0^{D_{max}} N(D) D^n dD'. \tag{7}$$

The mass-weighted mean diameter D_m (mm) is defined as the ratio of the fourth to the third moment of the size distribution as shown in (8):

$$D_m = \frac{M_4}{M_3}. \tag{8}$$

The generalized intercept parameter N_w (mm^{-1} m^{-3}) is given by

$$N_w = \frac{(4.0)^4}{\pi \rho_\omega} \left(\frac{10^3 W}{D_m^4} \right) \tag{9}$$

where ρ_ω (g cm^{-3}) is the density of water (1 g cm^{-3}), and W (g m^{-3}) is the rainwater content.

3. Overview of the Typhoon

Typhoon Mangkhut formed over the western north Pacific Ocean on 14 September 2018 and made landfall in Guangdong Province at 16:00 BST on 16 September 2018. Its maximum wind speed was 45 m s^{-1}, and its minimum central pressure was 955 hPa. It moved northwest at 25–30 km h^{-1}. The typhoon caused heavy rainfall in western Guangdong, eastern Guangdong, and the Pearl River Delta. The typhoon weakened and dissipated on 17 September 2018. During its passage over Guangdong, Typhoon Mangkhut passed through the disdrometer site.

The National Centers for Environmental Prediction's (NCEP) reanalysis data with a 0.25° × 0.25° spatial resolution at 08:00 BST on 16 September (Figure 2a,b), and the convective available energy (CAPE) for the three 2DVDs from the nearest sounding data at Yangjiang station and Heyuan station (Figure 2c,d) were used to analyze the precipitation system. The western Pacific subtropical high is

located in southern Japan (25° N–35° N) (Figure 2a). The airflow transported moisture and energy to Typhoon Mangkhut (Figure 2b). The main airflow came from the southeasterly jet from the Bay of Bengal, which is located near the equatorial convergence zone (5–15° N). The southeasterly jet continuously transported more moisture with a wind velocity greater than 7.5 m s^{-1} and a moisture flux divergence greater than 12 g cm^{-1} hPa^{-1} s^{-1}. The large moisture flux divergence in the typhoon's center was greater than 60 g cm^{-1} hPa^{-1} s^{-1}. In the outer rainband, before landfall (Figure 2c,d), the water vapor content was high in the lower layer and low at 850–700 hPa. The CAPE values at two stations were greater than 930 J kg^{-1}. The wind direction transitioned from northly near the ground layer to easterly in the low layer, transporting the warm, moist air in the atmospheric boundary layer. The dry, cold airflow in the mid-high level, the warm, moist airflow in the low level, and the high CAPE values were beneficial to thermal development [30–32].

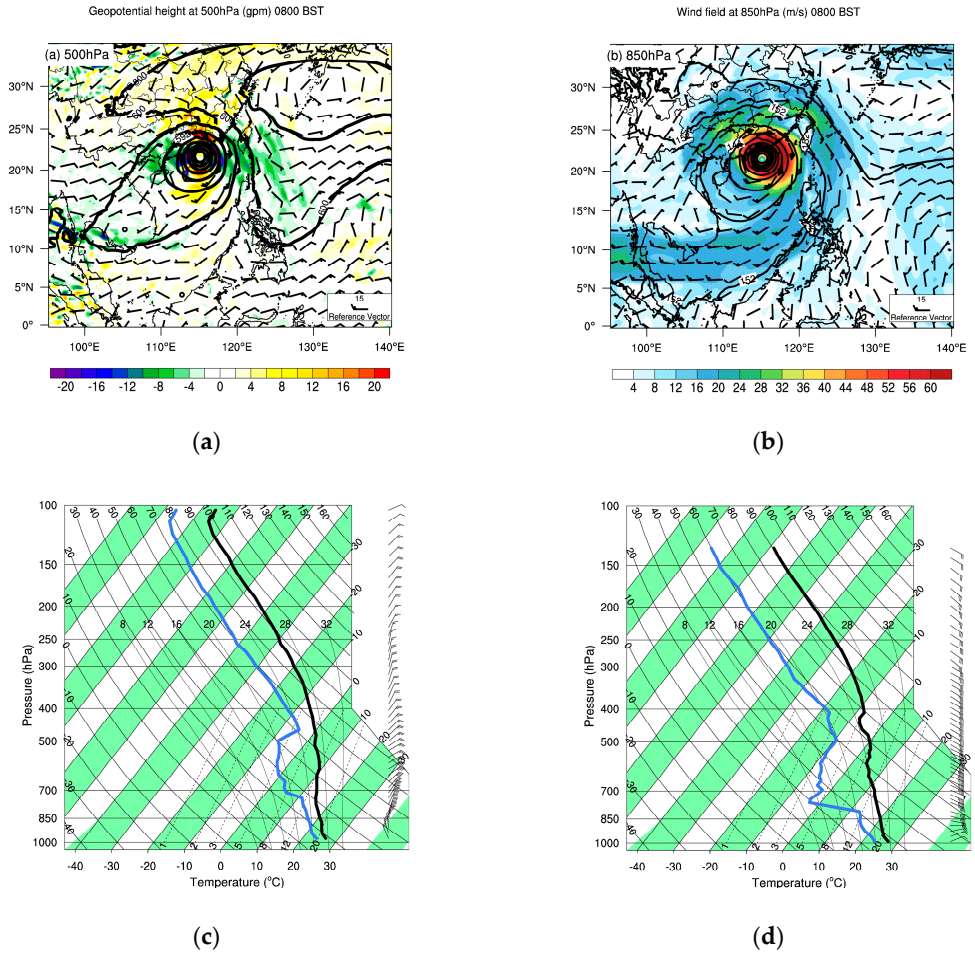

Figure 2. National Centers for Environmental Prediction reanalysis data with a 0.25° × 0.25° spatial resolution collected at 08:00 BST on September 16, 2018. (**a**) Vorticity field (10^{-5} s^{-1}) at 500 hPa, and (**b**) wind field and moisture flux divergence (g cm^{-1} hPa^{-1} s^{-1}) at 850 hPa. T–lnp curves for 06:00 BST on 16 September 2018 at (**c**) Yangjiang station and (**d**) Heyuan station.

Figure 3 shows the observed track of Typhoon Mangkhut and the radar reflectivity of the constant altitude plan position indicator (CAPPI) at an elevation angle of 0.5° at the GZ site based on the S-band polarimetric radar with a 200 km range. According to the observed track and the radar reflectivity, this process can be divided into three distinct segments: the outer rainband before landfall (S1), the inner core (S2), and the outer rainband after landfall (S3). To make it more clear, the movement direction and the direction perpendicular to the movement are shown in Figure 3b–e. It should be noted that during the passage of Typhoon Mangkhut, the time series of the disdrometer data at the

FG and XF sites reveal two different segments (S1 and S3) associated with these geographic positions. The standard to distinguish between S1 and S3 is whether the perpendicular (solid red arrow) passed the site or not. The specific time periods of the three segments at the three sites are presented in Table 1.

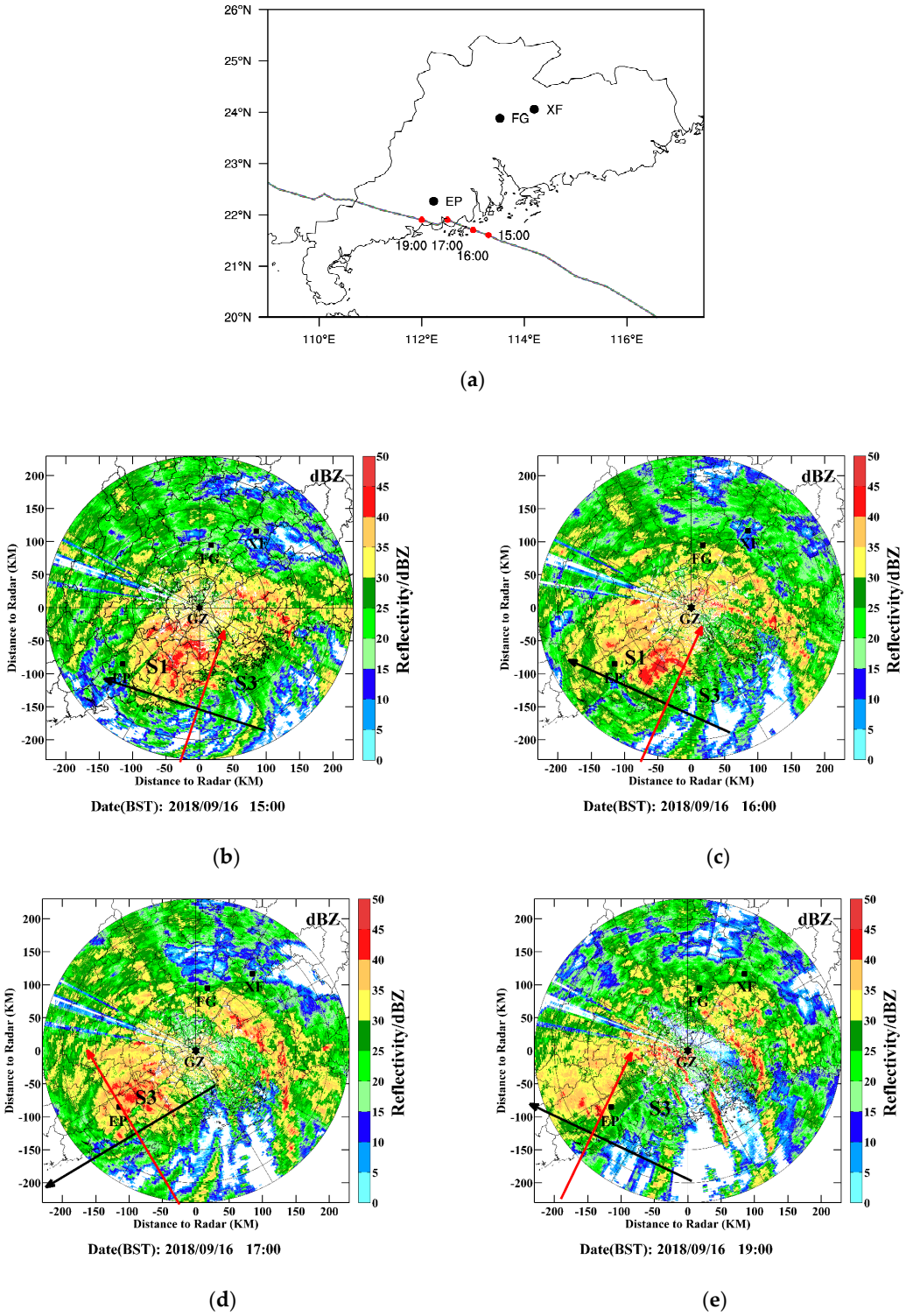

Figure 3. (**a**) Observed track of Typhoon Mangkhut, (**b**–**e**) radar reflectivity factor Z (dBZ) at 15:00 BST, 16:00 BST, 17:00 BST, and 19:00 BST, respectively. The solid black arrow is the movement direction of Typhoon Mangkhut. The solid red arrow is the direction perpendicular to the solid black arrow. The two lines intersect in the typhoon's eye.

Table 1. Duration of the three segments observed by the three 2DVDs.

Site	Segment	Period		Distance (km)
		Beginning	Ending	
EP	S1	09:00 BST, 16 Sep 2018	16:29 BST, 16 Sep 2018	223
	S2	16:30 BST, 16 Sep 2018	18:59 BST, 16 Sep 2018	58
	S3	19:00 BST, 16 Sep 2018	10:00 BST, 17 Sep 2018	260
FG	S1	09:00 BST, 16 Sep 2018	16:59 BST, 16 Sep 2018	301
	S3	17:00 BST, 16 Sep 2018	10:00 BST, 17 Sep 2018	402
XF	S1	09:00 BST, 16 Sep 2018	14:59 BST, 16 Sep 2018	328
	S3	15:00 BST, 16 Sep 2018	10:00 BST, 17 Sep 2018	451

Note: The terms S1, S2, and S3 represent the outer rainband before landfall, the inner core, and the outer rainband after landfall, respectively. The distance is that between the tropical cyclone's center and each disdrometer site (S1, S2, and S3).

The temporal variability of the instantaneous wind speed and the hourly rain rate at the EP, FG, and XF sites obtained from the National Ground Observation Station of China are shown in Figure 4. The maximum instantaneous wind speed (23.3 m s^{-1}) and the hourly rain rate (47.6 mm h^{-1}) occurred at the EP site during S2. Compared to S1, S3 had a lower instantaneous wind speed and a higher hourly rain rate.

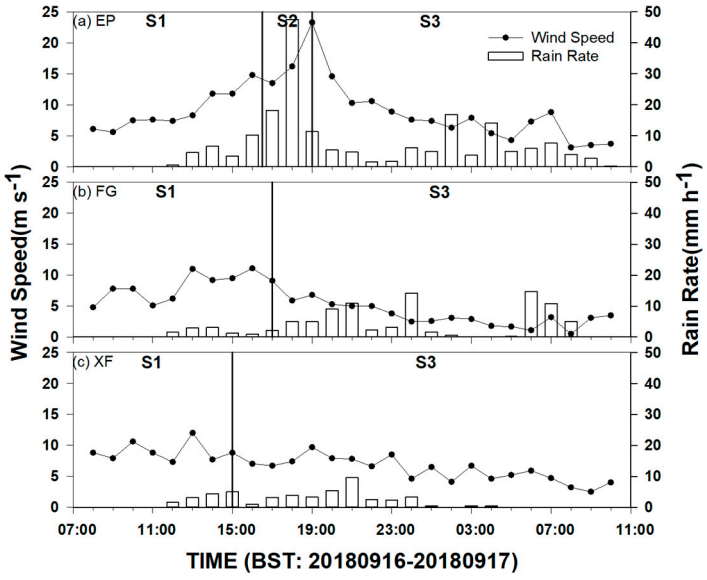

Figure 4. The temporal variabilities of the instantaneous wind speed and hourly rain rate obtained from the National Ground Observation Station of China at the (**a**) EP, (**b**) FG, and (**c**) XF sites.

In general, coastal Southern China was affected by a positive vorticity at 500 hPa, a low pressure at 850 hPa, and a high moisture content in the lower layer, which improved the development of the tropical cyclone. In addition, the wind was strong, and the rain rate was heavy during S2.

In the following sections, the characteristics of the DSDs during the three segments are analyzed to determine the microphysical process of Typhoon Mangkhut. The DSDs at the three sites are also compared to reveal any spatial variations.

4. DSDs Characteristics Derived from the 2DVD Measurements at the Three Stations

4.1. Temporal Evolution and Variations in the Raindrop Size Distribution (DSDs)

Figure 5 shows the time series of the DSDs observed by the three 2DVDs. The average DSD parameters for each segment are presented in Table 2. When we focused on the EP site (Figure 5a–c), we found that the evolution trends of the rain rate, radar reflectivity, and number concentration were consistent. The radar reflectivity and number concentration increase with increasing rain rate. Compared with the other segments, S1 exhibited the minimum radar reflectivity of 29.10 dBZ and mass-weighted mean diameter of 1.30 mm, and a relatively low rain rate (5.28 mm h^{-1}) and liquid water content (0.28 g m^{-3}) on average. The main characteristics of S1 were the relatively low concentrations of small and midsize drops (<3 mm) and the narrowest raindrop spectra (maximum diameter of about 3 mm). The raindrops with diameters of <1 mm, 1–3 mm, and >3 mm are defined as small, midsize, and large drops by Tokay et al. [27] and Janapati et al. [25]. We used the same size classification criteria in this study. After this, the precipitation system became stronger, and the rain rate initially increased and then decreased rapidly during S2. S2 exhibited the highest radar reflectivity of 34.53 dBZ, rain rate of 11.66 mm h^{-1}, liquid water content of 0.65 g m^{-3}, and number concentration of 4.12 mm^{-1} m^{-3} (on a logarithmic scale) on average. S2 was characterized by a high concentration of small and midsize drops (<3 mm) with a maximum diameter of about 3.9 mm. Finally, the precipitation system became weaker and the rain rate decreased slightly during S3. S3 exhibited the minimum rain rate of 5.05 mm h^{-1}, liquid water content of 0.26 g m^{-3}, and number concentration of 3.34 mm^{-1} m^{-3} (on a logarithmic scale) and the maximum mass-weighted mean diameter of 1.52 mm. The DSDs showed a high concentration of small and midsize drops (<3 mm) with a larger diameter (about 4 mm).

The time series of DSDs showed the same characteristic at the FG and XF sites (Figure 5d–i). First, the precipitation system was weak, and the rain rate varied slightly during S1. S1 exhibited a low rain rate, liquid water content, and number concentration. The maximum concentration of the small drops was about 4 mm^{-1} m^{-3} (on a logarithmic scale). Then, the precipitation system became stronger and the rain rate increased slightly during S3. The maximum concentration of the small drops increased to about 5 mm^{-1} m^{-3} (on a logarithmic scale) during S3. Compared with S1, S3 was characterized by a higher concentration of small and midsize drops (<3 mm) with a maximum diameter of about 5 mm.

In general, the DSDs at the three sites exhibited some similar characteristics during the three segments. During S1, they experienced weak precipitation and a smaller maximum diameter (<3 mm). During S2, they experienced strong precipitation with the highest number concentration of small and midsize drops (<3 mm) with a maximum diameter of about 3.9 mm. During S3, they exhibited a maximum diameter of about 4.0 mm and a high number concentration of small drops (<1 mm).

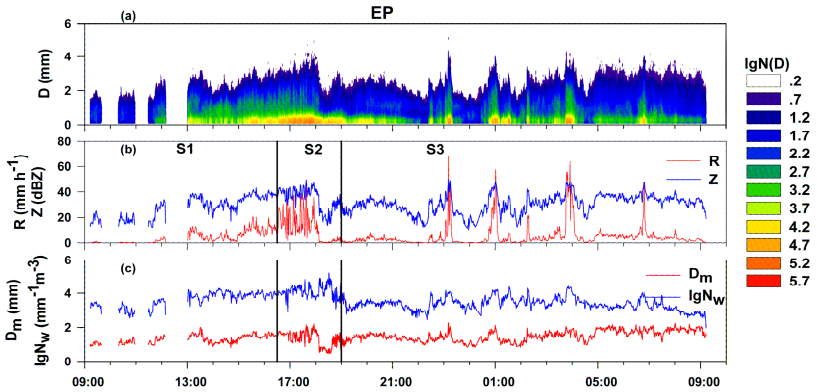

Figure 5. *Cont.*

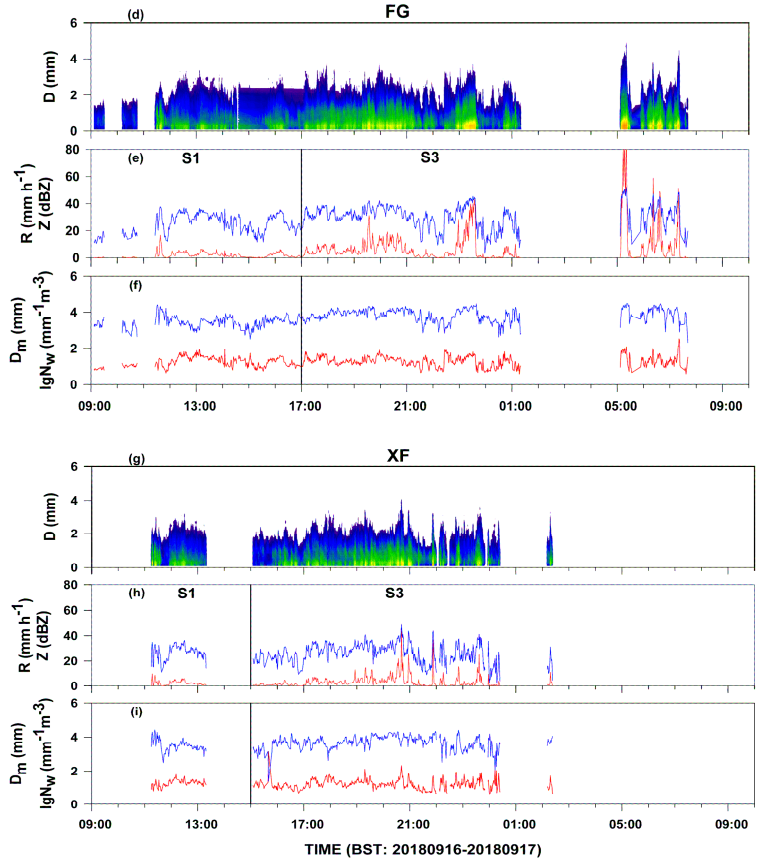

Figure 5. Temporal evolution of the number concentration ND (mm^{-1} m^{-3}, shown by lgND), rain rate R (mm h^{-1}), radar reflectivity factor Z (dBZ), mass-weighted mean diameter D_m (mm), and normalized number concentration N_w (mm^{-1} m^{-3}, shown by the lgN_w) at the (**a**–**c**) EP, (**d**–**f**) FG, and (**g**–**i**) XF sites.

Table 2. Microphysical characteristics of the raindrop size distributions of the three segments of Typhoon Mangkhut at the three sites. The 1st/2nd/3rd values are the means, medians, and standard deviations for specific periods, respectively.

Site	Segment	R (mm h^{-1})	Z (dBZ)	D_m (mm)	lgN_w (mm^{-1} m^{-3})	LWC (g m^{-3})
EP	S1	5.28/3.57/4.83	29.10/37.31/7.97	1.30/1.30/0.24	3.66/3.77/0.41	0.28/0.23/0.24
	S2	11.66/9.12/11.02	34.53/43.97/8.84	1.33/1.48/0.44	4.12/4.12/0.38	0.65/0.59/0.55
	S3	5.05/2.84/8.44	30.88/38.90/6.98	1.52/1.51/0.31	3.34/3.38/0.36	0.26/0.16/0.42
FG	S1	2.06/1.50/2.11	25.40/33.01/6.89	1.24/1.21/0.27	3.46/3.46/0.30	0.12/0.10/0.11
	S3	6.36/4.24/11.98	29.99/38.70/8.34	1.28/1.29/0.29	3.82/3.91/0.35	0.35/0.25/0.57
XF	S1	2.42/1.97/1.85	27.34/35.23/5.37	1.29/1.29/0.19	3.50/3.47/0.32	0.14/0.11/0.11
	S3	3.45/1.94/4.68	26.26/33.74/7.66	1.21/1.20/0.29	3.68/3.72/0.38	0.19/0.13/0.23

Note: The terms R, Z, D_m, lgN_w, and LWC are the rain rate, radar reflectivity, mass-weighted mean diameter, normalized number concentration, and liquid water content, respectively.

4.2. DSD Parameters

Scatterplots of the shape parameter (μ), mass-weighted mean diameter (D_m), slope parameter (Λ), and total concentration (N_t) versus the rain rate (R) for the three segments are shown in Figure 6. Segments S1, S2, and S3 are shown as red dots, green dots, and blue dots, respectively. The range decreases with increasing rain rate, and it becomes more stable at higher rain rates at the EP site (Figure 6a). The values of μ and Λ decrease, while D_m and N_t increase with the increasing rain rate. The differences between the three segments are significant. When R < 10 mm h^{-1}, the ranges of μ, D_m,

Λ, and N_t are greater during S1 and S3. This indicates that the microphysical process is complicated during S1 and S3. When R > 25 mm h^{-1}, during S2 and S3, the values of μ and Λ remain nearly constant, and the values of D_m converge, while the values of N_t increase with the increasing rain rate. In addition, when R > 25 mm h^{-1}, there were no raindrops measured by the 2DVD during S1. For high rain rates, the raindrop size distributions evolve into an equilibrium distribution under the action of coalescence and breakup [33]. Under these equilibrium conditions, the value of D_m remains nearly constant, and the increase in the raindrop concentration is mainly due to the increase in the rain rate [18]. When we focused on the probability density function (PDF), we found that the majority of the raindrop sizes (D_m) were 1–2 mm in three segments. The distributions of the four parameters have the same characteristics for the FG and XF sites (Figure 6b,c). The difference is that there were no raindrops at the XF site when R > 60 mm h^{-1}. This is probably because of the different location. The characteristics of D_m and N_t in our study show that the heavy precipitation in the typhoon was mainly composed of high concentrations of small and midsize drops (<2 mm), which is consistent with the results of Chang et al. [17], Wen et al. [20], and Janapati et al. [25].

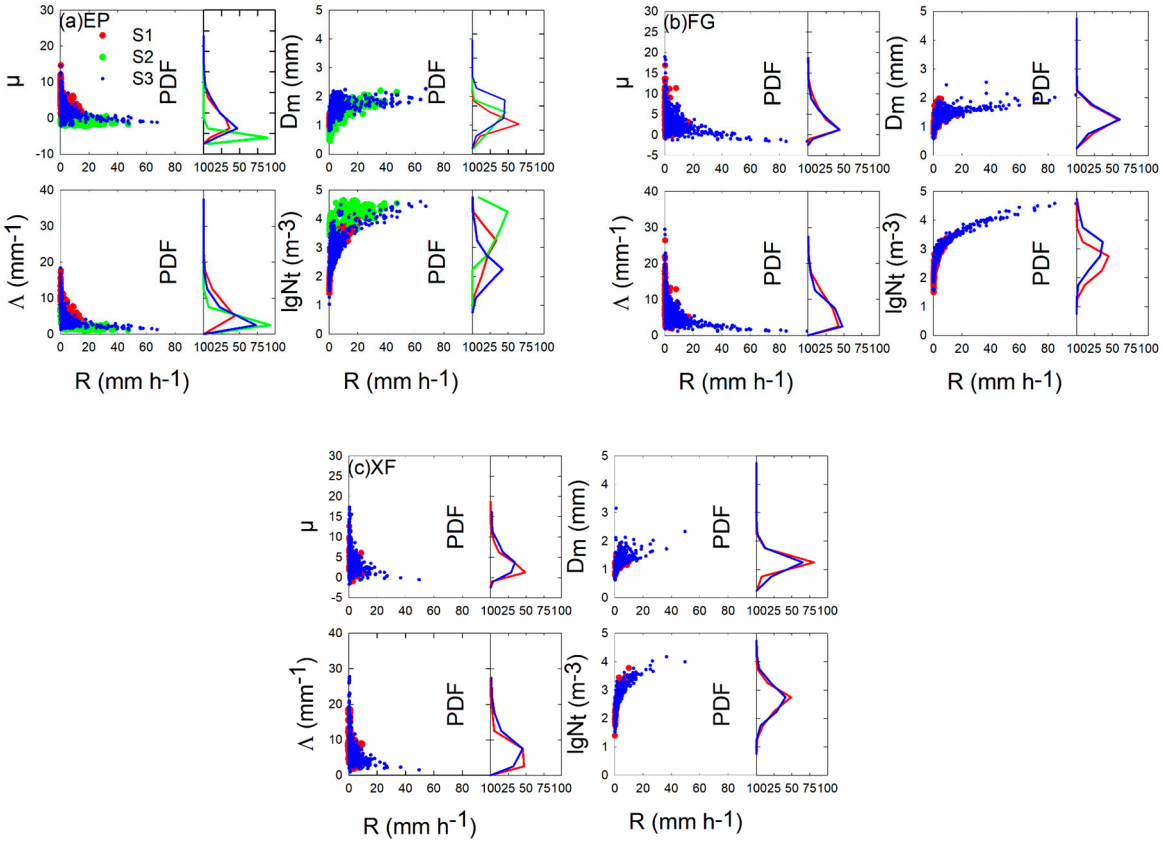

Figure 6. Scatterplots of μ, D_m (mm), Λ (mm^{-1}), and lgN_t (m^{-3}) versus R (mm h^{-1}) for the three segments at the (**a**) EP, (**b**) FG, and (**c**) XF sites. The probability density functions (PDF) of the four raindrop size distribution (DSD) parameters at the EP, FG, and XF sites are given in each panel as well. Segments S1, S2, and S3 are shown as red dots, green dots, and blue dots, respectively.

To make it clearer, Figure 7 shows the relative contribution of each size class to the total raindrop concentration (N_t) and R. The relative contributions of N_t and R at the EP site show that the small drops (<1 mm) dominate N_t (>90%) and the midsize drops (1–2 mm) dominate R (>45%) in all three segments. When we focused on the small drops (<1 mm), we found that the relative contributions of N_t and R initially increased and then decreased from S1 to S3. More significantly, the drops that were 1–3 mm in diameter contributed to the rain rate in S2. The large drops (>4 mm) contributed less than 3% during S2 and S3, and their contribution was negligible during S1. Except for the larger size

drops (4 mm), the relative contributions of N_t and R at the three sites exhibit similar behaviors. This is consistent with the conclusion drawn from Figure 6 that the small and midsize drops dominated the typhoon's precipitation.

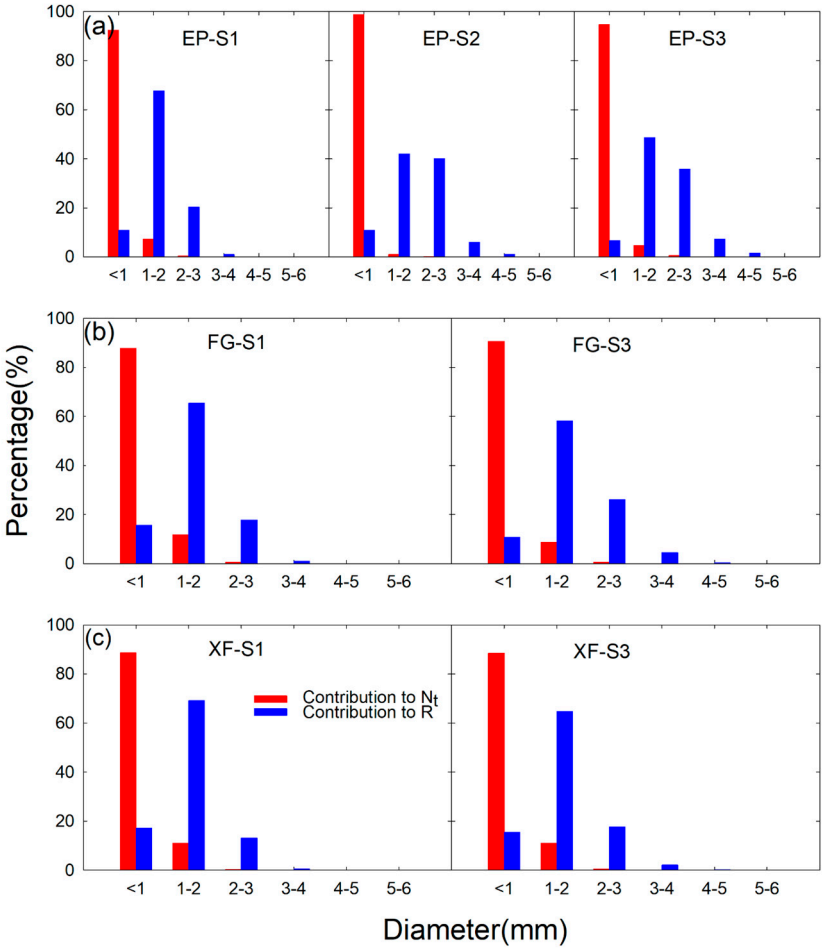

Figure 7. Relative contribution of each size class to the total raindrop concentration N_t (red) and rain rate R (blue) for the entire dataset at the (**a**) EP, (**b**) FG, and (**c**) XF sites.

Overall, the characteristics of the DSD parameters were different in the three segments because of the different dynamic and thermodynamic mechanisms of rain formation in the different rain regions [34–37]. As a result of the different locations, the characteristics of the DSD parameters in the same segment were not completely the same for the EP, FG, and XF sites. In the following section, the characteristics of the DSDs during the three segments are investigated.

5. Gamma and DSD Parameters of the Three Segments

5.1. Distributions of D_m and N_w

Previous studies have shown that because of the different microphysical processes during rain formation, the DSDs of different rain types vary [38–41]. The variations in the N_w–D_m values reflect the different microphysical formation mechanisms [18]. The percentage occurrence of the various rain types, which were classified using Bao's method [21], is given in Figure 8. Figure 8 shows that during S1 (S3), the stratiform rain contributed more than 70% (50%), while the convective rain contributed more than 60% during S2. Lin et al. [26] also reported that the typhoon precipitation in the eye wall region was mainly produced by convective rain. In addition, the distributions of the mass-weighted mean diameter D_m and the generalized number concentration N_w in the three segments are shown in

Figure 9. The maritime-like (continental-like) cluster has D_m values of 1.5–1.75 mm (2–2.75 mm) and lgN_w values of 4–4.5 (3–3.5 mm^{-1} m^{-3}) (the two gray rectangles in Figure 9) for the convective rain, as defined by Bringi et al [18].

The mean D_m steadily increases, and the mean of the logarithmic N_w (lgN_w) increases initially and then decreases from S1 to S3 (Figure 9a). The variance of D_m increases initially and then decreases, and lgN_w steadily increases. When we focused on S1 (Figure 9b), we found that the lgN_w–D_m pairs mainly occur to the left of the stratiform line defined by Bringi et al. [18] due to the strong stratiform rain over the three sites (Figure 8). During S2, it was mainly composed of convective rain. The lgN_w–D_m pairs show an inhomogeneous distribution with few pairs falling in the maritime-like cluster, while some of the pairs have D_m values of 0–1.25 mm and lgN_w values of 4.5–5.0 mm^{-1} m^{-3}. During S3, we found that the lgN_w–D_m pairs were evenly distributed around the stratiform line due to the contribution of stratiform raindrops. Interestingly, few lgN_w–D_m pairs fall in the maritime-like cluster, and fewer lgN_w–D_m pairs fall in the continental-like cluster. This also indicates that the number of lgN_w–D_m pairs that fall in the maritime-like cluster increases from S2 to S3 because of the abundant moisture brought from the South China Sea by the typhoon.

The mean D_m and lgN_w values of tropical cyclones in different parts of China are presented in Table 3. The grade of the tropical cyclone reported by the Japan Meteorological Agency (JMA) (http://www.jma.go.jp/jma/index.html) is also presented in Table 3. Typhoon Mangkhut (typhoon) has a smaller raindrop diameter than and the same generalized number concentration as Typhoon Matmo (extra-tropical cyclone), which is the strongest tropical cyclone in Table 3. When we focused on the same grade of tropical cyclone (typhoon), we found that our D_m is slightly larger than that of Typhoon Morakot in Fujian, while our D_m (lgN_w) is larger (smaller) than that of Typhoon Hato, which made landfall in Guangdong. However, if we compare our D_m and lgN_w values with those of Typhoon Nida and Typhoon Pakhar (severe tropical storm), which made landfall in Guangdong, our lgN_w is smaller and our D_m is in between those of the other two. The sufficient water vapor brought by the typhoon from the ocean may influence the values of the DSD parameters (such as lgN_w and D_m). Moreover, the strong winds shown in Figure 4 may have suppressed the collision–coalescence and breakup of the raindrops.

Table 3. Mean D_m and lgN_w values and μ–Λ relationship of various tropical cyclones in different regions.

Region	Grade	Name	Author	D_m	lgN_w	μ–Λ Relationship
Eastern China	Extra-tropical Cyclone	Matmo	Wang et al. 2016	1.41	4.67	$\mu = -0.021\Lambda^2 + 1.075\Lambda - 2.979$
Taiwan, China	Typhoon + Tropical Storm	Two Tropical Cyclones	Chang et al. 2009	2	3.8	$\Lambda = 0.0136\mu^2 + 0.6984\mu + 1.5131$
Fujian, China	Typhoon	Morakot	Chen et al. 2012	1.30	–	$\Lambda = 0.0253\mu^2 + 0.633\mu + 1.524$
Guangdong, China	Severe Tropical Storm	Nida	Wen et al. 2018	1.4	4.5	–
Guangdong, China	Typhoon	Hato	Wen et al. 2018	1.2	4.8	–
Guangdong, China	Severe Tropical Storm	Pakhar	Wen et al. 2018	1.3	4.7	–
Eastern + southern China	Severe Tropical Storm + Typhoon	Seven Tropical Cyclones	Wen et al. 2018	–	–	$\mu = -0.019\Lambda^2 + 1.09\Lambda - 3.119$
Guangdong, China	Rainstorm	–	Liu et al. 2019	1.66	3.91	$\Lambda = 0.0241\mu^2 + 0.867\mu + 2.453$
Guangdong, China	Typhoon	Mangkhut	This study	1.33	4.12	$\mu = -0.0306\Lambda^2 + 1.3513\Lambda - 3.145$

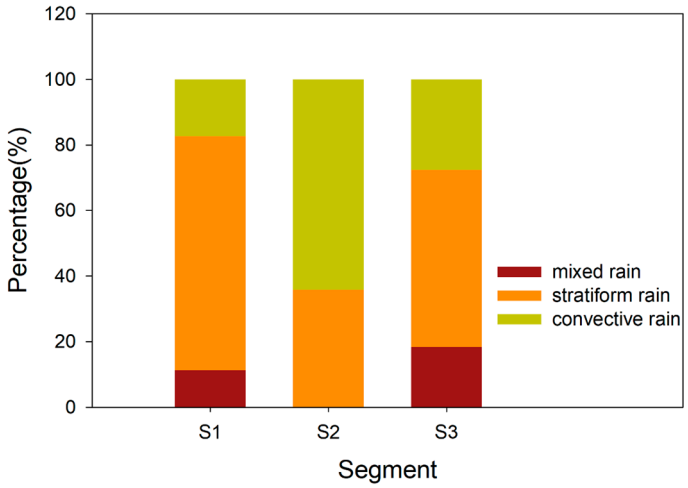

Figure 8. The percentage occurrence of the different rain types in the three segments.

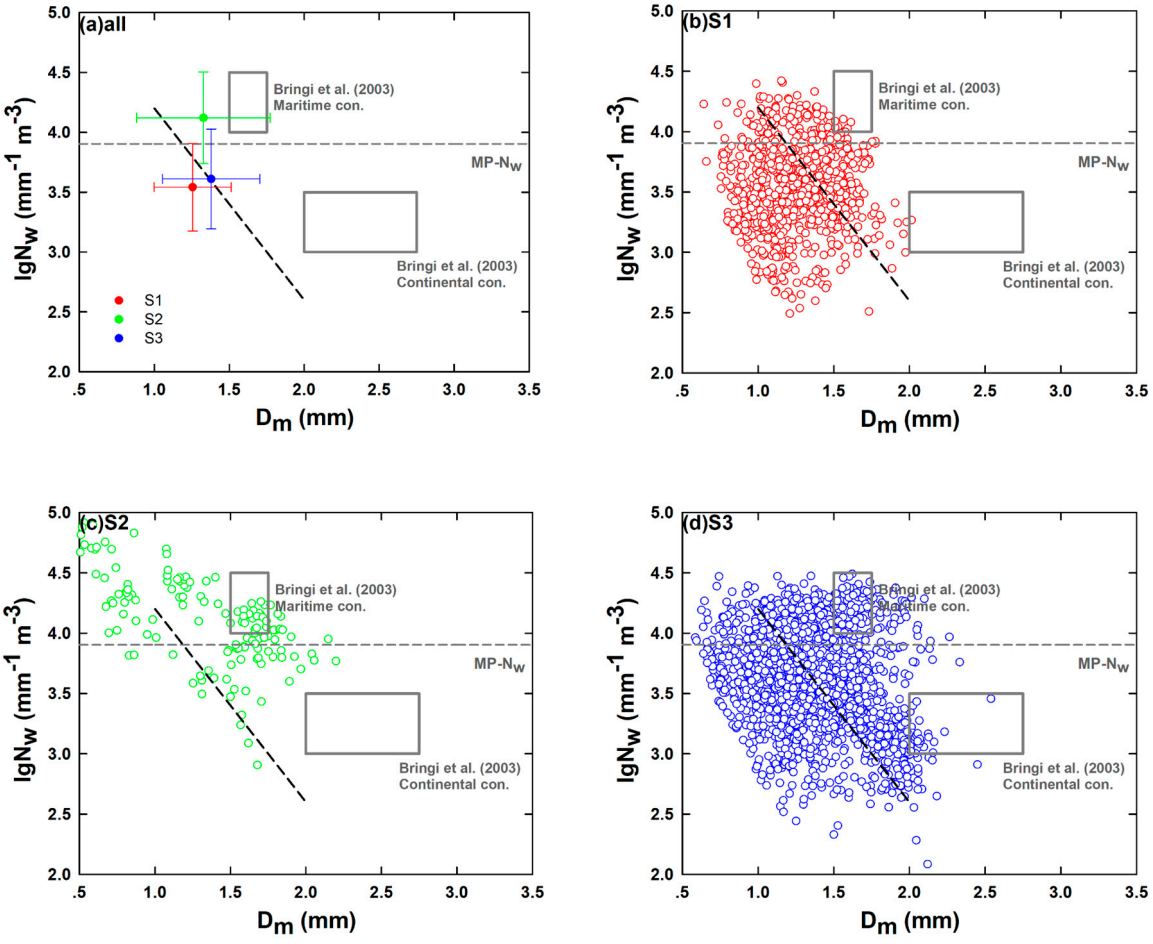

Figure 9. (**a**) The mean and variance of the mass-weighted mean diameter D_m (mm) and the generalized number concentration N_w (mm^{-1} m^{-3}) for the entire dataset. Scatterplot of D_m and N_w (**b**) during S1, (**c**) during S2, and (**d**) during S3. The black dotted line is the regression relationship of Bringi et al. (2003) for stratiform rain. The two gray rectangles are the maritime-like and continental-like clusters of Bringi et al. (2003).

5.2. μ–Λ Relationship

The three-parameter (N_0, μ, and Λ) gamma distribution is important to understanding the DSD characteristics [42,43]. The parameters μ and Λ are the shape and slope of the DSD, respectively. Furthermore, the μ–Λ relationship is useful for retrieving the DSD parameters and rain parameters from the remote measurements [41,44]. These μ–Λ relationships are dependent on the geographic location, climate, and rain type [43,45]. Thus, it is necessary to investigate the μ–Λ relationships in each region. To minimize the error, the sample data with rain rates of < 5 mm h^{-1} and total concentrations of N_t <1000 were removed [43]. The μ–Λ relationship (Figure 10) shows that there is a good relationship between μ and Λ. The μ–Λ relationship in this study was fitted using the polynomial least squares method. Compared with the other observation results listed in Table 3, our μ–Λ relationship is closest to that developed by Liu et al. [13] for heavy rainfall in Guangdong. In contrast, there are considerable differences among the μ–Λ relationships developed by scholars for different parts of China [16,17,19,20,43]. This indicates that the μ–Λ relationship depends on geographic location, climate, and rain type, which is consistent with the conclusions of previous studies. In addition, the μ–Λ relationship differs from that developed by Zhang et al. [43], which has been widely used to calculate the DSD parameters retrieved from polarimetric radar observations [42,46,47]. We also found that the majority of the μ–Λ pairs are characterized by μ< 0 and Λ< 2.5 mm^{-1} during S2, while they were characterized by μ> 0 and Λ ≈ 2.5–6 mm^{-1} during S1 and S3. This indicates that the microphysical processes during S1 and S3 were complicated, which is similar to the result obtained in Section 4.2.

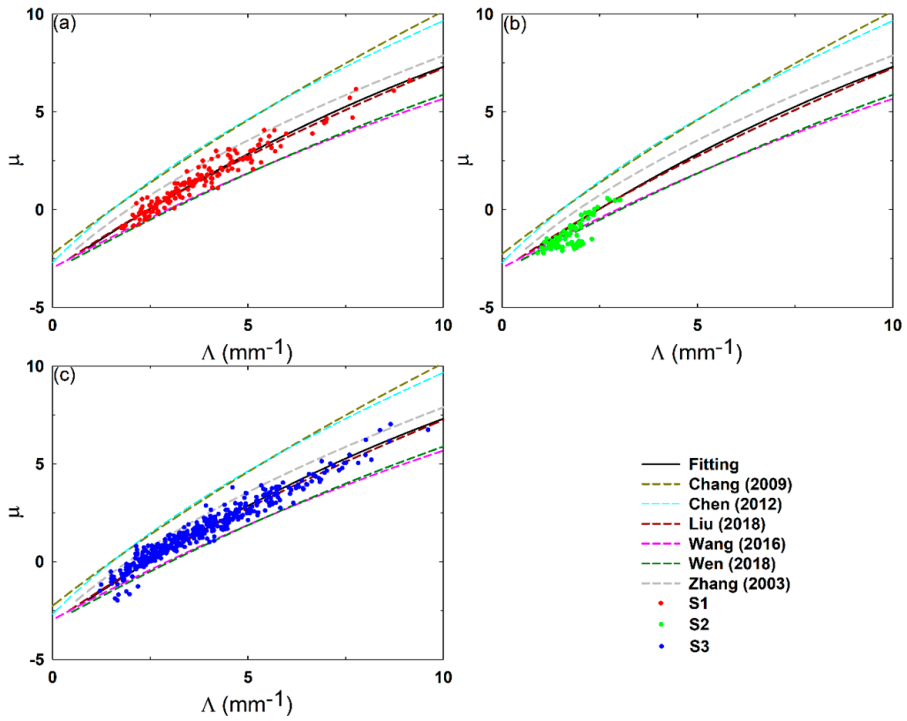

Figure 10. Scatterplots of the μ–Λ relationships during (**a**) S1, (**b**) S2, and (**c**) S3. S1, S2, and S3 are shown as red dots, green dots, and blue dots, respectively. The black lines denote the fitting curves of the filtered samples. In addition, the μ–Λ relationships from Chang (2009), Chen (2012), Liu (2018), Wang (2016), Wen (2018), and Zhang (2003) are provided. S1: the outer rainband before landfall, S2: the inner core, S3: the outer rainband after landfall.

5.3. Raindrop Spectra

The raindrop spectra of the three segments (Figure 11) show a high concentration of small drops (<0.5 mm). During S2, the number concentration within each size bin is larger than those of the other

segments, especially the small drops (<0.5 mm) and large drops (>4 mm), resulting in a heavy rain rate. The spectrum is wider and has a lager maximum drop diameter (5.3 mm) during S2 and S3. During the passage of the typhoon, the size spectrum changes from narrow to wide, and the evolution of the number concentration initially increases and then decreases.

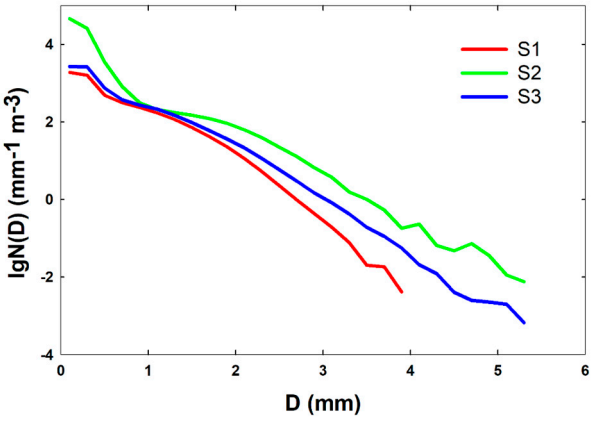

Figure 11. Raindrop spectra of the three segments.

6. Summary

In this study, the microphysical characteristics of the DSDs during the passage of Typhoon Mangkhut were investigated using the 2DVD data collected from the Longmen Field Experiment Base for Cloud Physics, China Meteorological Administration. Based on the observed track and radar reflectivity, this process can be divided into three distinct segments (S1–S3). Moreover, the time evolution of the raindrop size distribution reflects the different segments. This study mainly focused on the characteristics of the DSDs during the three segments to determine the microphysical processes of Typhoon Mangkhut. The DSDs at the three different sites were compared to reveal any spatial variations. In addition, the microphysical characteristics of Typhoon Mangkhut were compared with those of other tropical cyclones in different parts of China. The DSDs of Typhoon Mangkhut exhibit different characteristics in the three segments. During segment S2, the mean of the mass-weighted mean diameter (D_m) was 1.33 mm, while the variance of the D_m was larger (0.44) than in the other segments, and the mean of the generalized number concentration (lgN_w) was 4.12 mm^{-1} m^{-3}, which is the largest value among the three segments.

1. During segment S1 (the outer rainband before landfall), the circulation moved northwestward. A strong stratiform precipitation episode mixed with convective precipitation lasting more than 2 h occurred over all three sites. The maximum drop size was less than 3 mm, and the raindrop concentration was less than 4 mm^{-1} m^{-3} (on a logarithmic scale) at all three sites. The small and midsize drops mainly contributed to the rain rate. The lgN_w–D_m pairs mainly occurred to the left of the stratiform line.
2. During segment S2 (the inner core), a strong convective precipitation process occurred over site EP. This segment had the largest instantaneous wind speed (23.3 m s^{-1}), rain rate (11.66 mm h^{-1}), radar reflectivity (34.53 dBZ), liquid water content (0.65 g m^{-3}), and number concentration (4.12 mm^{-1} m^{-3} in logarithmic scale) on average. The small drops (<1 mm) mainly contributed to the number concentration, while the small and midsize drops (1–3 mm) mainly contributed to the rain rate. The N_w–D_m scatter pairs indicate maritime-like convection.
3. During segment S3 (the outer rainband after landfall), a widespread stratiform precipitation episode mixed with convective precipitation lasted above 10 h. The DSDs were characterized by a high concentration of small drops (<1 mm) and a few larger drops (>5 mm). The maximum drop

size was greater than 4 mm at all three sites. The N_w–D_m points were mostly distributed around the stratiform rain area, with a few points falling in both the maritime-like and continental-like clusters.

This study indicates that the three segments had different DSD characteristics. The outer rainband mainly produced stratiform rains, while the inner core mainly produced convective rains. The small and midsize drops (<3 mm) dominated the typhoon precipitation. The shape (μ) and slope (Λ) exhibit a good polynomial least squares relationship.

In addition, the mean values of D_m and lgN_w were quite different among the tropical cyclones in different parts of China. Compared with the stronger tropical cyclone (Typhoon Matmo) in Eastern China, our D_m and lgN_w were smaller (1.33 mm and 4.12 mm^{-1} m^{-3}, respectively). The values of the DSD parameters (such as D_m and lgN_w) may be influenced by the sufficient water vapor brought by the tropical cyclone from the ocean and strong winds of the tropical cyclone.

The DSDs of Typhoon Mangkhut, which made landfall in Southern China, were quite different from those of tropical cyclones in other parts of China and even within the same region. Therefore, further tropical cyclones making landfall in Southern China are worth investigating in the future.

Author Contributions: Conceptualization, S.H. and X.L.; Investigation, L.F. and H.X.; Supervision, X.L., H.X. and X.P.; Formal analysis, X.P., F.X., G.O. and C.Z.; Writing—original draft preparation, L.F.; Writing—review and editing, L.F. All authors have read and agreed to the published version of the manuscript.

Funding: This research was funded by Science and Technology Planning Project of Guangdong Province, China (2017B020244002), the National Natural Science Foundation of China (41975138, 41705120, 41705011, 41905047), and the Natural Science Foundation of Guangdong Province, China (2019A1515010814, 2018A030313969).

Acknowledgments: We thank YUE Qian for translating the manuscript. We also acknowledge LI Jin-hong, WANG Jian-zhuang and LIU Huang for their assistance in the field experiment. This research was jointly supported by Science and Technology Planning Project of Guangdong Province, China (2017B020244002), the National Natural Science Foundation of China (41975138, 41705120, 41705011, 41905047), and the Natural Science Foundation of Guangdong Province, China (2019A1515010814, 2018A030313969).

Conflicts of Interest: The authors declare no conflict of interest.

References

1. Kirankumar, N.V.P.; Rao, T.N.; Radhakrishna, B.; Rao, D.N. Statistical characteristics of raindrop size distribution in southwest monsoon season. *J. Appl. Meteorol. Clim.* **2008**, *47*, 576–590. [CrossRef]
2. Tao, W.K.; Lang, S.; Zeng, X.P.; Li, X.W.; Matsui, T.; Mohr, K.; Posselt, D.; Chern, J.; Christa, P.L.; Peter, M.N.; et al. The Goddard Cumulus Ensemble model (GCE): Improvements and applications for studying precipitation processes. *Atmos. Res.* **2014**, *143*, 392–424. [CrossRef]
3. Chen, H.; Chandrasekar, V.; Bechini, R. An Improved dual–polarization radar rainfall algorithm (DROPS2.0): Application in NASA IFloodS field campaign. *J. Hydrol.* **2017**, *18*, 917–937. [CrossRef]
4. Liu, L.P.; Ge, R.S.; Zhang, P.Y. A study of method and accuracy of rainfall rate and liquid water content measurements by dual linear polarization doppler radar. *Chin. J. Atmos Sci.* **2002**, *26*, 709–720. [CrossRef]
5. Gong, X.H.; Zhu, D.L.; Zhang, L.; Zhang, Y.S.; Ge, M.S.; Yang, W. Drop size distribution of fixed spray-plate sprinklers with two-dimensional video disdrometer. *Trans. Chin. Soc. Agric. Mach.* **2014**, *45*, 128–133. (In Chinese) [CrossRef]
6. Clardy, D.E.; Tolbert, C.W. Electronic disdrometer. *Rev. Sci. Instrum.* **1961**, *32*, 916–919. [CrossRef]
7. Frasson, R.P.D.M.; Cunha, L.K.D.; Krajewski, W.F. Assessment of the Thies optical disdrometer performance. *Atmos. Res.* **2011**, *101*, 237–255. [CrossRef]
8. Hauser, D.; Amayenc, P.; Nutten, B.; Waldteufel, P. New optical instrument for simultaneous measurement of raindrop diameter and fall speed distributions. *J. Atmos. Ocean. Technol.* **1909**, *1*, 256–269. [CrossRef]
9. Kinnell, P.I.A. Some observations on the Joss–Waldvogel rainfall disdrometer. *J. Appl. Meteorol.* **1976**, *15*, 499–502. [CrossRef]
10. Nystuen, J.A. Listening to raindrops from underwater: An acoustic disdrometer. *J. Atmos. Ocean. Technol.* **2001**, *18*, 1640–1657. [CrossRef]
11. Raupach, T.H.; Berne, A. Correction of raindrop size distributions measured by Parsivel disdrometers, using a two–dimensional video disdrometer as a reference. *Atmos. Meas. Tech.* **2015**, *8*, 343–365. [CrossRef]

12. Kruger, A.; Krajewski, W.F. Two–dimensional video disdrometer: A description. *J. Atmos. Ocean. Technol.* **2002**, *19*, 602–617. [CrossRef]
13. Liu, X.T.; Wan, Q.L.; Wang, H.; Xiao, H.; Zhang, Y.; Zheng, T.F.; Feng, L. Raindrop size distribution parameters retrieved from Guangzhou S–band polarimetric radar observations. *J. Meteorol. Res.* **2018**, *32*, 571–583. [CrossRef]
14. Wen, L.; Zhao, K.; Zhang, G.F.; Xue, M.; Zhou, B.W.; Liu, S.; Chen, X.C. Statistical characteristics of raindrop size distributions observed in East China during the Asian summer monsoon season using 2–D video disdrometer and Micro Rain Radar data. *J. Geophys. Res. Atmos.* **2016**, *121*, 2265–2282. [CrossRef]
15. Tokay, A.; Bashor, P.G.; Habib, E.; Kasparis, T. Raindrop size distribution measurements in tropical cyclones. *Mon. Weather Rev.* **2008**, *136*, 1669–1685. [CrossRef]
16. Chen, B.J.; Wang, Y.; Ming, J. Microphysical characteristics of the raindrop size distribution in Typhoon Morakot (2009). *J. Trop. Meteorol.* **2012**, *18*, 162–171. [CrossRef]
17. Chang, W.Y.; Wang, T.C.C.; Lin, P.L. Characteristics of the raindrop size distribution and drop shape relation in typhoon systems in the western pacific from the 2D video disdrometer and NCU C–band polarimetric radar. *J. Atmos. Ocean. Technol.* **2009**, *26*, 1973–1993. [CrossRef]
18. Bringi, V.N.; Chandrasekar, V.; Hubbert, J.; Gorgucci, E.; Randeu, W.L.; Schoenhuber, M. Raindrop size distribution in different climatic regimes from disdrometer and dual–polarized radar analysis. *J. Atmos. Sci.* **2003**, *60*, 354–365. [CrossRef]
19. Wang, M.J.; Zhao, K.; Xue, M.; Zhang, G.F.; Liu, S.; Wen, L.; Chen, G. Precipitation microphysics characteristics of a Typhoon Matmo (2014) rainband after landfall over eastern China based on polarimetric radar observations. *J. Geophys. Res. Atmos.* **2016**, *121*, 12415–12433. [CrossRef]
20. Wen, L.; Zhao, K.; Chen, G.; Wang, M.J.; Zhou, B.W.; Huang, H.; Hu, D.M.; Lee, W.C.; Hu, H.F. Drop size distribution characteristics of seven typhoons in China. *J. Geophys. Res. Atmos.* **2018**, *123*, 6529–6548. [CrossRef]
21. Bao, X.W.; Wu, L.G.; Tang, B.; Ma, L.M.; Wu, D.; Tang, J.; Chen, H.J.; Wu, L.Y. Variable raindrop size distributions in different rainbands associated with typhoon fitow (2013). *J. Geophys. Res. Atmos.* **2019**, *124*, 12262–12281. [CrossRef]
22. Zhang, Y.; Liu, L.P.; Wen, H.; Chen, C.; Wang, H.; Xi, B.Z. Development and assessment of quantitative precipitation estimation algorithms for S–, C–, and X–band dual–polarization radars based on disdrometer data from three regions of China. *J. Trop. Meteorol.* **2019**, *25*, 269–292. [CrossRef]
23. Niu, S.J.; Jia, X.C.; Sang, J.R.; Liu, X.L.; Lu, C.S.; Liu, Y.G. Distributions of raindrop sizes and fall velocities in a semiarid plateau climate: Convective versus stratiform rains. *J. Appl. Meteorol. Climatol.* **2010**, *49*, 632–645. [CrossRef]
24. Luo, L.; Xiao, H.; Yang, H.L.; Chen, H.N.; Guo, J.; Sun, Y.; Feng, L. Raindrop size distribution and microphysical characteristics of a great rainstorm in 2016 in Beijing, China. *Atmos. Res.* **2020**, *239*, 104895. [CrossRef]
25. Janapati, J.; Seela, B.K.; Reddy, M.V.; Reddy, K.K.; Lin, P.-L.; Rao, T.N.; Liu, C.-Y. A study on raindrop size distribution variability in before and after landfall precipitations of tropical cyclones observed over southern India. *J. Atmos. Sol. Terr. Phys.* **2017**, *159*, 23–40. [CrossRef]
26. Lin, W.; Chen, S.; Hu, Y.J.; Li, D. The characteristics of RSDs before and after the Landing Typhoon Meranti. *Trop. Cyclone Res. Rev.* **2020**. [CrossRef]
27. Tokay, A.; Petersen, W.A.; Gatlin, P.; Wingo, M. Comparison of raindrop size distribution measurements by collocated disdrometers. *J. Atmos. Ocean. Technol.* **2013**, *30*, 1672–1690. [CrossRef]
28. Feng, L.; Xia, F.; Wang, Q.L.; Xiao, H.; Liu, X.T.; Zheng, T.F.; Li, H.Q. Characteristics of the raindrop size distribution in two squall lines measured by Two–dimensional video disdrometer at Guangdong. *J. Trop. Meteorol.* **2019**, *35*, 812–821. (In Chinese) [CrossRef]
29. Ulbrich, C.W. Natural variations in the analytical form of the raindrop size distribution. *Clim. Appl. Meteorol.* **1983**, *22*, 1764–1775. [CrossRef]
30. Weisman, M.L.; Klemp, J.B.; Rotunno, R. Structure and evolution of numerically simulated squall lines. *J. Atmos. Sci.* **1988**, *45*, 1990–2013. [CrossRef]
31. Xu, F.; Zheng, Y.Y.; Xiao, H.; Mu, X.Y. Mesoscale characterstics of a severe hail event over the area along Yangtze River in Jiangsu. *Meteorol. Mon.* **2016**, *42*, 567–577. (In Chinese) [CrossRef]

32. Li, Z.; Zhang, Y.T.; Liu, Q.J.; Fu, S.Z.; Ma, Z.S. A Study of the Influence of Microphysical Processes on Typhoon Nida (2016) Using a New Double-moment Microphysics Scheme in the Weather Research and Forecasting Model. *J. Trop. Meteorol.* **2018**, *24*, 123–130. [CrossRef]
33. Hu, Z.L.; Srivastava, R.C. Evolution of raindrop size distribution by coalescence, breakup, and evaporation: Theory and observations. *J. Atmos. Sci.* **1995**, *52*, 1761–1783. [CrossRef]
34. Black, R.A.; Hallett, J. Electrification of the hurricane. *J. Atmos. Sci.* **1999**, *56*, 2004–2028. [CrossRef]
35. Houze, R.A. Clouds in tropical cyclones. *Mon. Weather Rev.* **2010**, *138*, 293–344. [CrossRef]
36. Houze, R.A.; Marks, F.D.; Black, R.A. Dual-aircraft investigation of the inner core of hurricane norbert. Part II: Mesoscale distribution of ice particles. *J. Atmos. Sci.* **1992**, *49*, 943–963. [CrossRef]
37. Marks, F.D.; Houze, R.A. Airborne doppler radar observations in hurricane debby. *Bull. Am. Meteorol. Soc.* **1984**, *65*, 569–582. [CrossRef]
38. Brown, B.R.; Bell, M.M.; Frambach, A.J. Validation of simulated hurricane drop size distributions using polarimetric radar. *Geophys. Res. Lett.* **2016**, *43*, 910–917. [CrossRef]
39. Krajewski, W.F.; Kruger, A.; Caracciolo, C.; Golé, P.; Barthes, L.; Creutin, J.-D.; Delahaye, J.Y.; Nikolopoulos, E.I.; Ogden, F.; Vinson, J.-P. DEVEX–disdrometer evaluation experiment: Basic results and implications for hydrologic studies. *Adv. Water Resour.* **2006**, *29*, 311–325. [CrossRef]
40. Lee, C.K.; Lee, G.W.; Zawadzki, I.; Kim, K.E. A preliminary analysis of spatial variability of raindrop size distributions during stratiform rain events. *J. Appl. Meteorol. Clim.* **2009**, *48*, 270–283. [CrossRef]
41. Zhang, G.; Vivekanandan, J.; Brandes, E. A method for estimating rain rate and drop size distribution from polarimetric radar measurements. *IEEE Trans. Geosci. Remote Sens.* **2001**, *39*, 830–841. [CrossRef]
42. Brandes, E.A.; Zhang, G.F.; Vivekanandan, J. Drop size distribution retrieval with polarimetric radar: Model and application. *J. Appl. Meteorol.* **2004**, *43*, 461–475. [CrossRef]
43. Zhang, G.F.; Vivekanandan, J.; Brandes, E.A.; Meneghini, R.; Kozu, T. The shape-slope relation in observed gamma raindrop size distributions: Statistical error or useful information? *J. Atmos. Ocean. Technol.* **2003**, *20*, 1106–1119. [CrossRef]
44. Ding, Y.; Wan, Q.L.; Yang, L.; Liu, X.T.; Xia, F.; Feng, L. Raindrop size distribution parameters retrieved from xinfeng c-band polarimetric radar observations. *J. Trop. Meteorol.* **2020**, *26*, 275–286. [CrossRef]
45. Janapati, J.; Seela, B.K.; Lin, P.-L.; Wang, P.K.; Tseng, C.-H.; Reddy, K.K.; Hashiguchi, H.; Feng, L.; Das, S.K.; Unnikrishnan, C.K. Raindrop size distribution characteristics of Indian and Pacific Ocean tropical cyclones observed at India and Taiwan sites. *J. Meteorol. Soc. Jpn.* **2020**, *98*, 299–317. [CrossRef]
46. Brandes, E.A.; Zhang, G.F.; Vivekanandan, J. An evaluation of a drop distribution-based polarimetric radar rainfall estimator. *J. Appl. Meteorol.* **2003**, *42*, 652–660. [CrossRef]
47. Brandes, E.A.; Zhang, G.F.; Vivekanandan, J. Comparison of polarimetric radar drop size distribution retrieval algorithms. *J. Atmos. Ocean. Technol.* **2004**, *21*, 584–598. [CrossRef]